Phase-Dependent Electronic Structure Modulation of Nickel Selenides by Fe Doping for Enhanced Bifunctional Oxygen Electrocatalysis

Vigneshraaj A S[a,b], Siva Kumar Ramesh[c], Jinkwon Kim[c], Kavita Pandey*[a,b]

[a]Centre for Nano and Soft Matter Sciences (CeNS), Shivanapura, Bengaluru 562162, India

[b]Academy of Scientific and Innovative Research (AcSIR), Ghaziabad, 201002, India

[c]Department of Chemistry, Kongju National University,56 Gongjudaehak-ro, Gongju-si, Chungnam-do 32588, South Korea

Corresponding author: E-mail: kavitapandey@cens.res.in

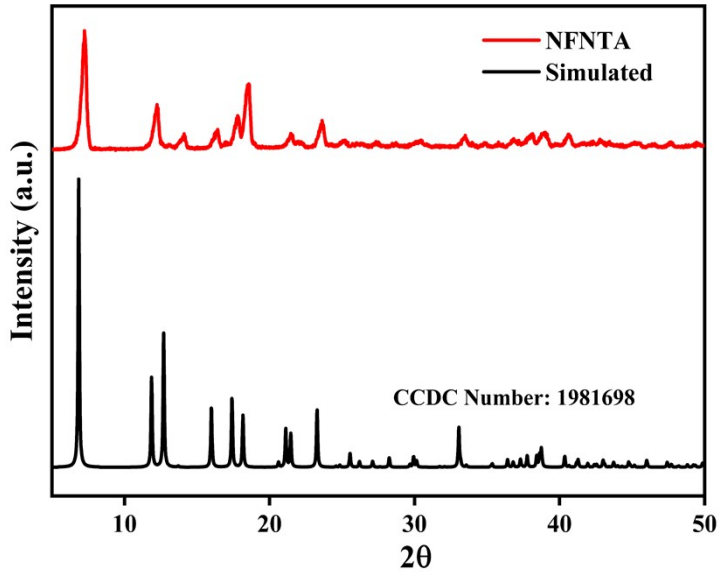

Figure S1. XRD pattern of NiFe-NTA

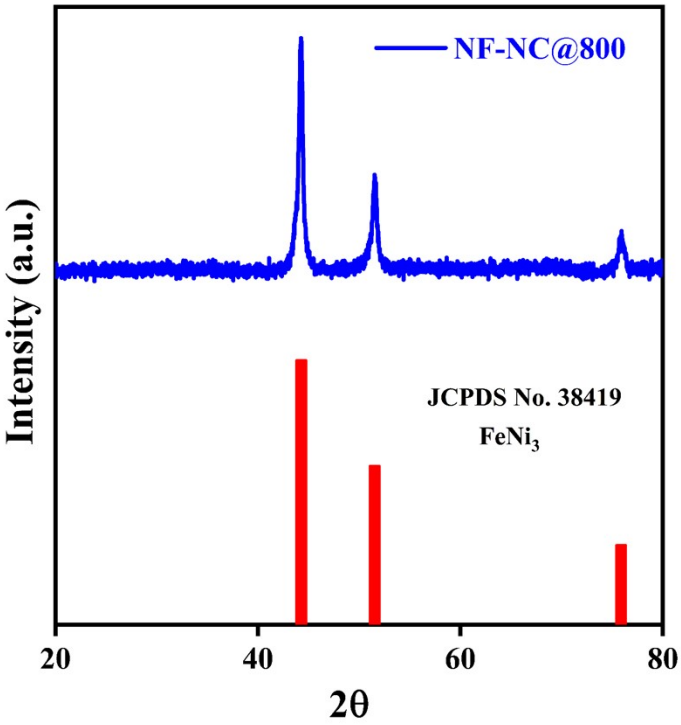

Figure S2. XRD pattern of NiFe-NC-800

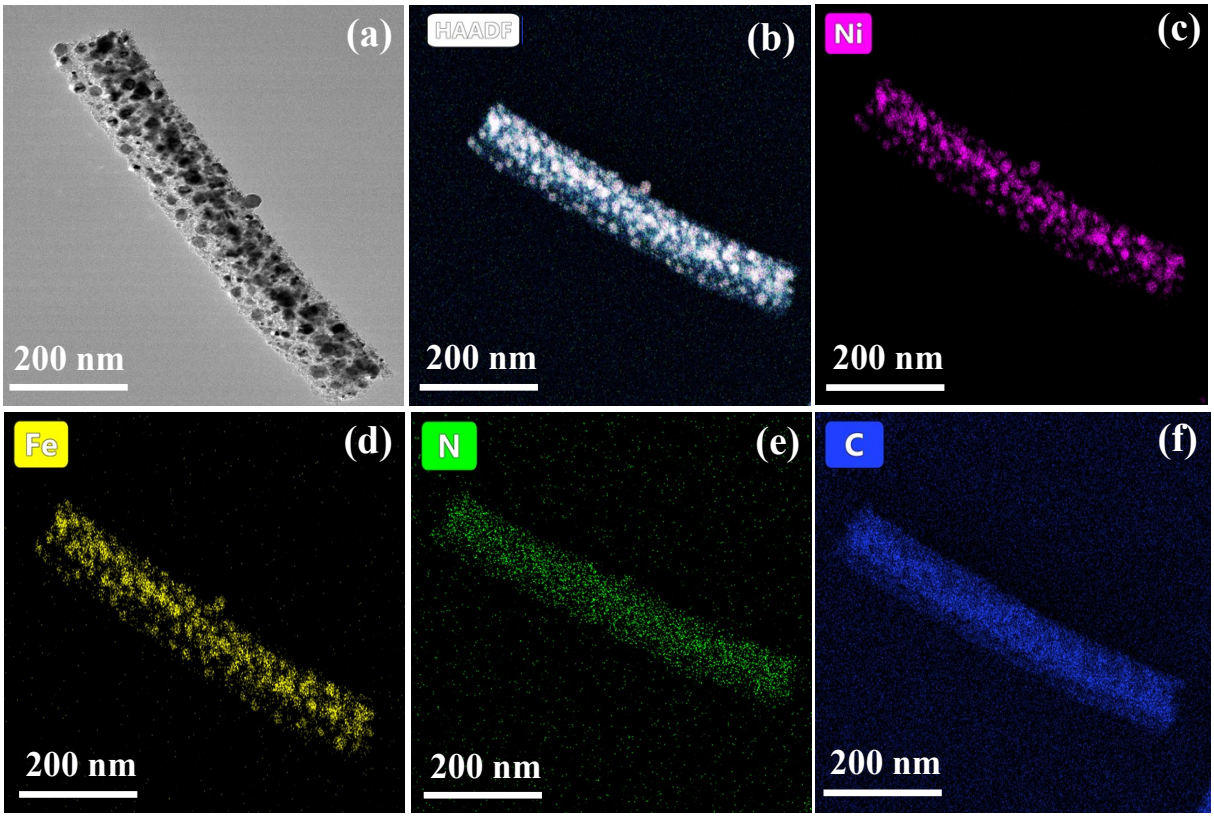

Figure S3. (a) TEM images of NF-NC@800 (b-f) HAADF-Elemental mapping of $Ni_{3-x}Fe_xSe_4$-NC@550

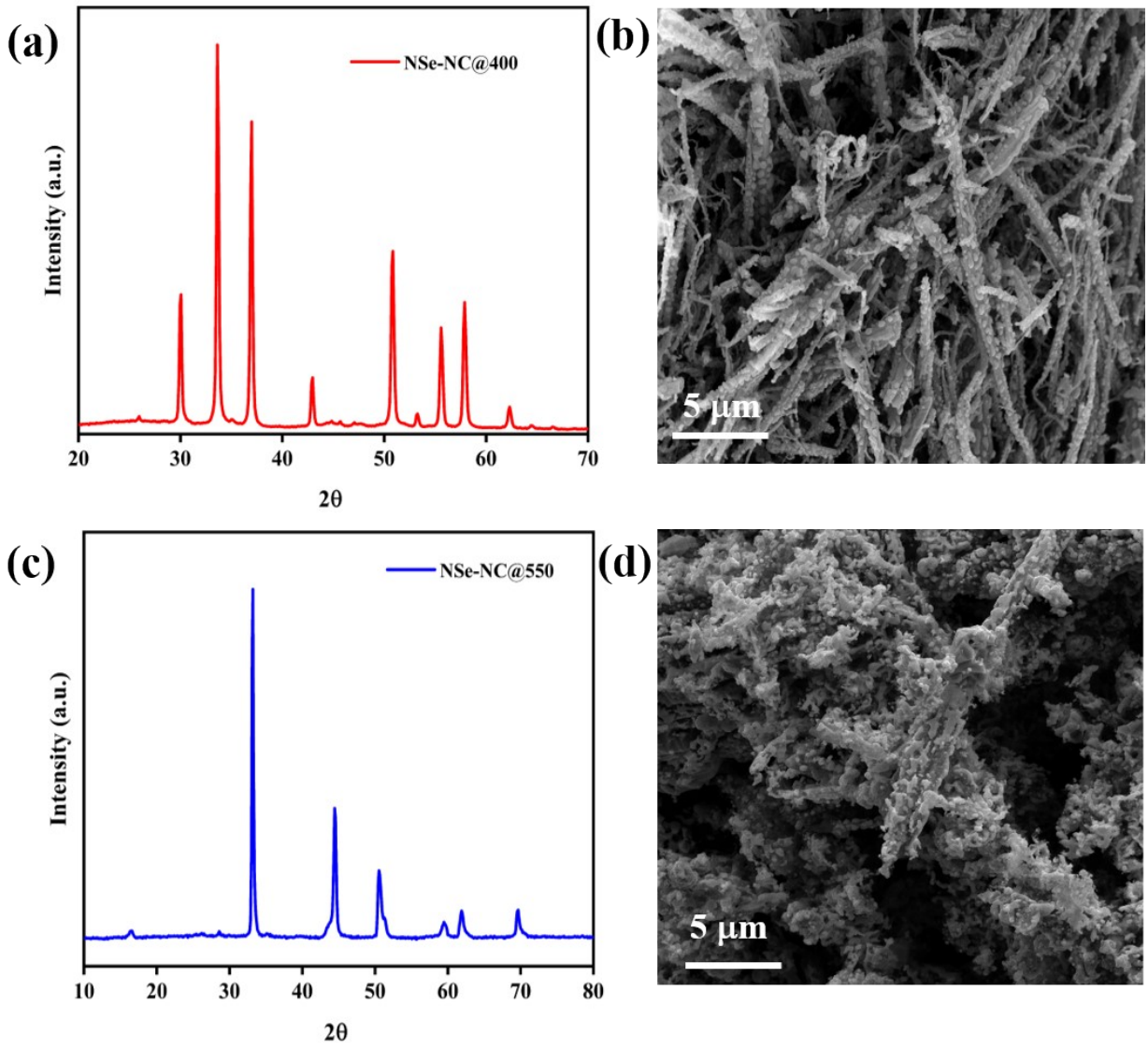

Figure S4. XRD pattern and FESEM images of (a, b) $NiSe_2$-NC@400, and (c,d) Ni_3Se_4-NC@550

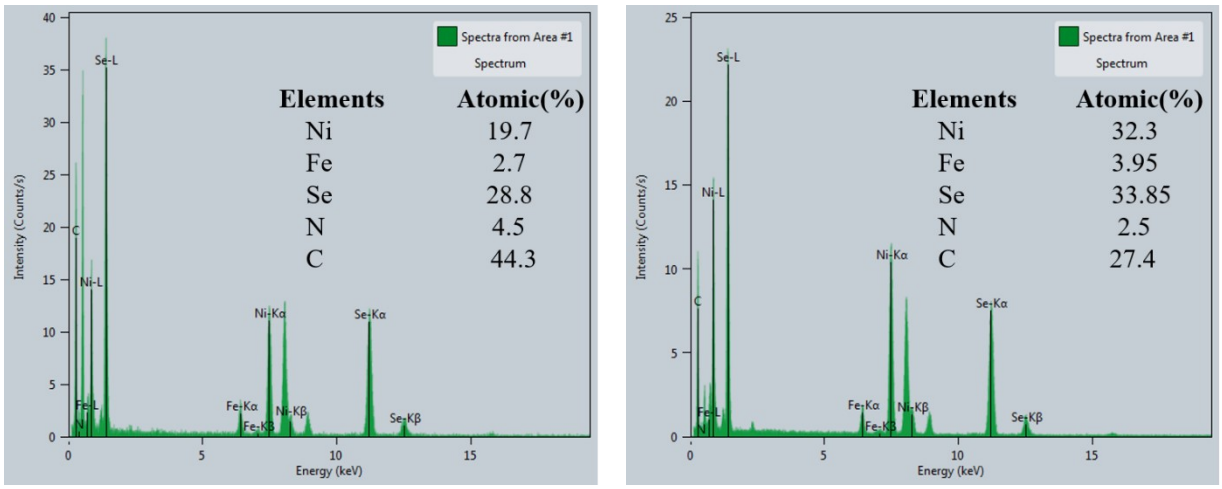

Fig. S5. EDAX images of (a.) NFSe-NC@400 (b.) NFSe-NC@550

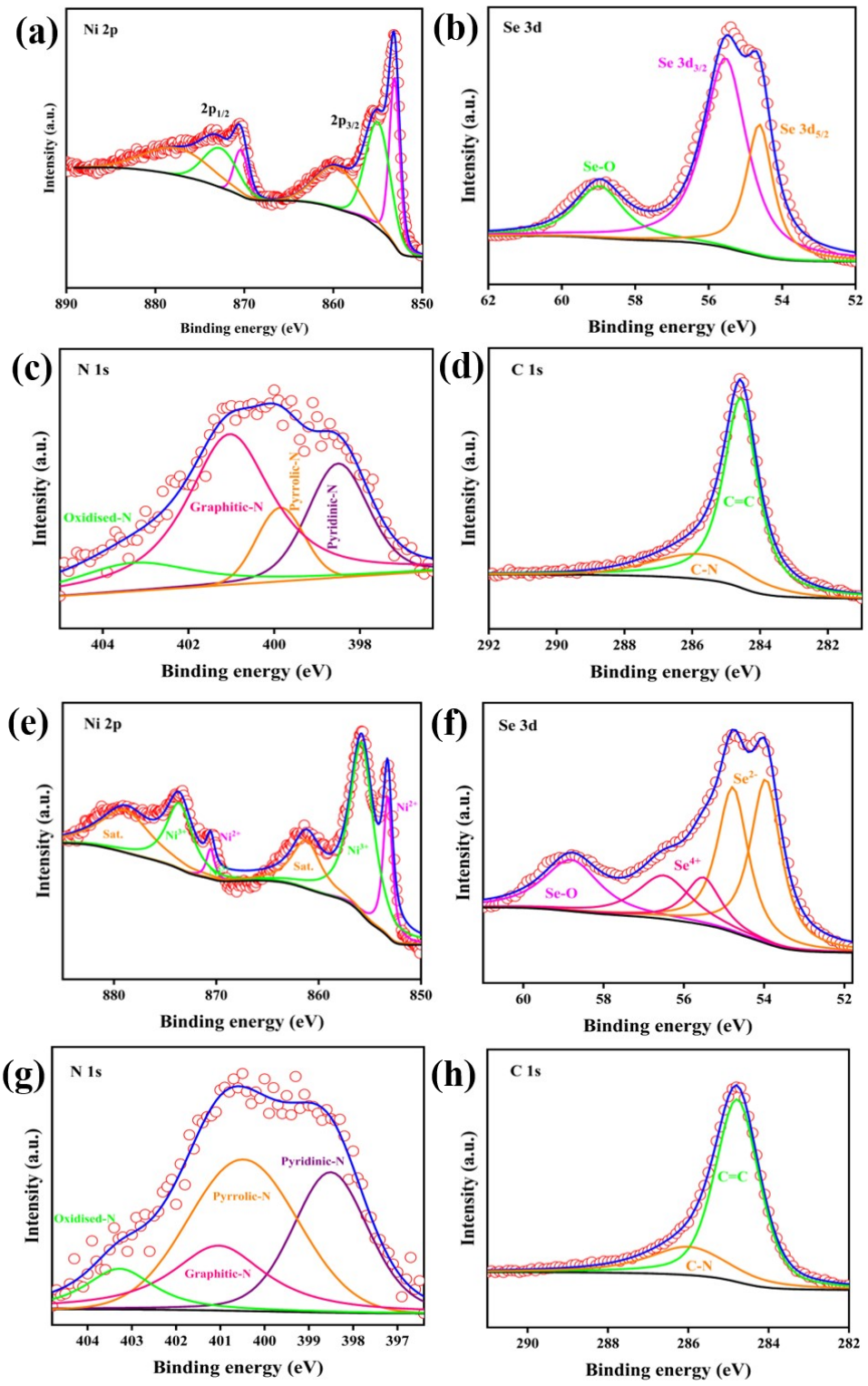

Figure S6. XPS spectra of (a,e) Ni 2p, (b,f) Se 3d, (c,g) N 1s, (d,h) C 1s of NSe-NC@400 and NSe-NC@550

XPS analysis of NSe-NC@400, and NSe-NC@550:

Further, Ni 2p of NSe-NC@400 (Fig.S6a), which has $NiSe_2$ phase without Fe doping, is deconvoluted and has six peaks, including two satellite peaks at 877.5 and 859.8 eV. As indicated in Figure S6a, two peaks attributed at 853.4 and 870.5 eV represent Ni^{2+} ions and two more peaks centered at 855.4 and 872.6 eV represent oxidized Ni peaks. Further, Se 3d (Figure S6b), N 1s (Figure S6c), and C 1s (Figure S6d) of NSe-NC@400 are in a similar fashion to NFSe-NC@400. The Ni2p of NSe-NC@550 is also deconvoluted into six peaks, and $Ni2p_{3/2}$ is centered at 855.8 and 853.2 eV corresponds to Ni^{3+} and Ni^{2+} and Ni $2p_{1/2}$ centered at 873.6 and 870.5 eV represents Ni^{3+} and Ni^{2+} respectively. As shown in Figure S6e, Ni2p has two more peaks representing the satellite peak at 861.2 and 878.8 eV. Further, Se 3d (Figure S6f), N 1s (Figure S6g), and C 1s (Figure S6h) of NSe-NC@550 were similar in fashion to NFSe-NC@550.

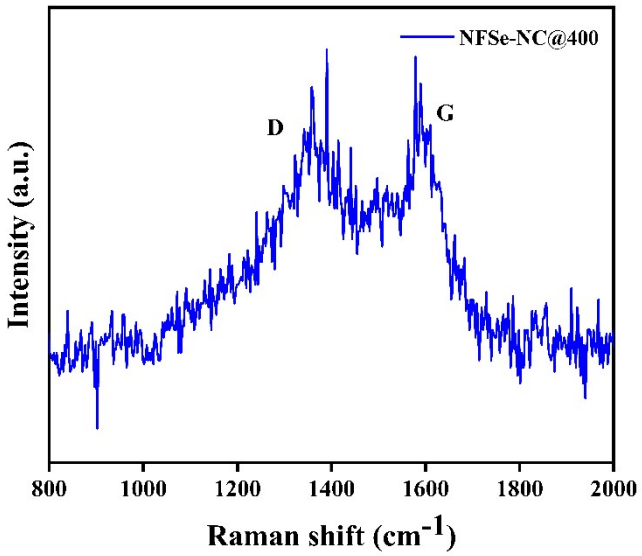

Figure S7. Raman spectra of NFSe-NC@400

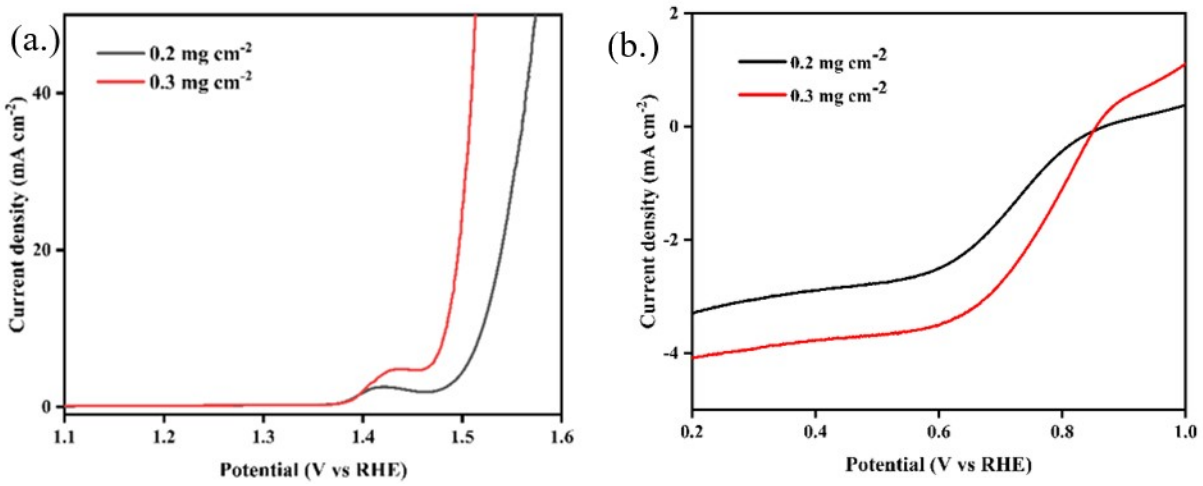

Figure S8. Effect of mass loading of NFSe-NC@400 (a.) OER (b.) ORR

The increment of mass loading tends to higher electrocatalytic OER and ORR activity.[1,2]

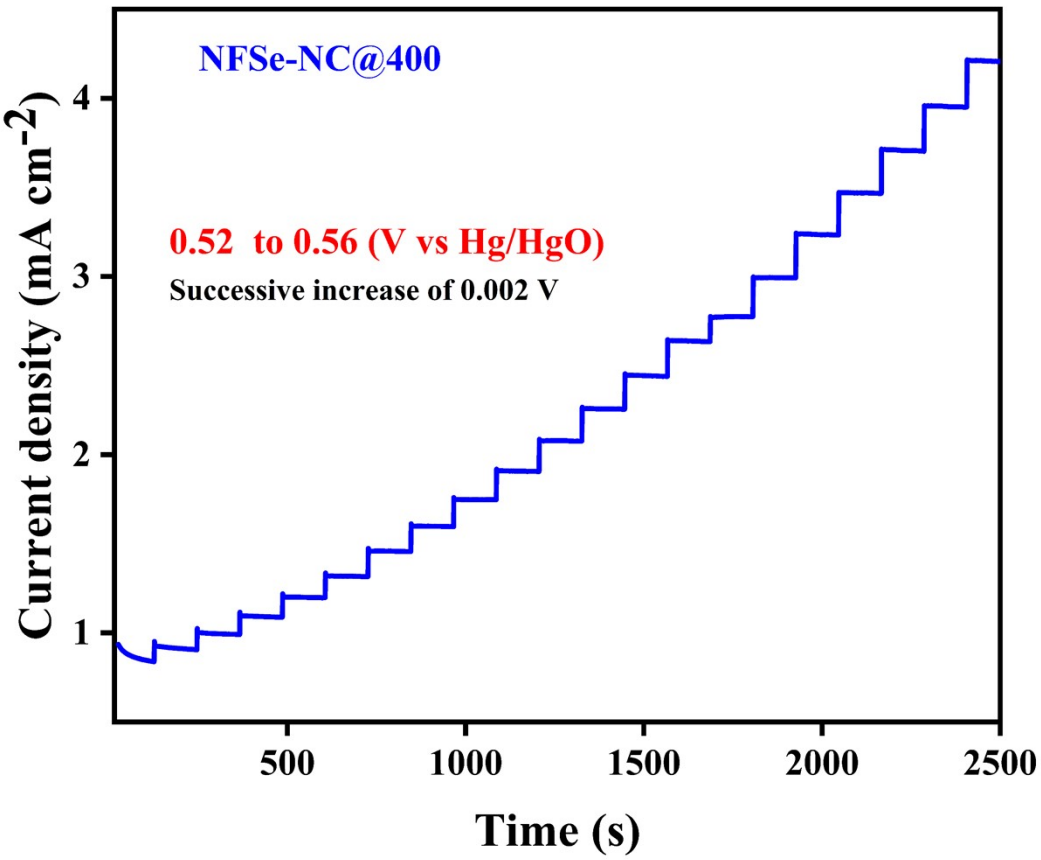

Figure S9. CA study of NFSe-NC@400 for Tafel slope in the catalytic turnover region

Chronoamperometry (steady state) is used to determine the Tafel analysis, as the polarization curve does not represent the steady state.[3]

So, we used CA for analyzing the tafel plot for all samples. It shows the CA study from 0.52 to 0.56 V (vs Hg/HgO) of NFSe-NC@400 for the successive increase of 0.002V. Similarly, we have done CA for all other samples.

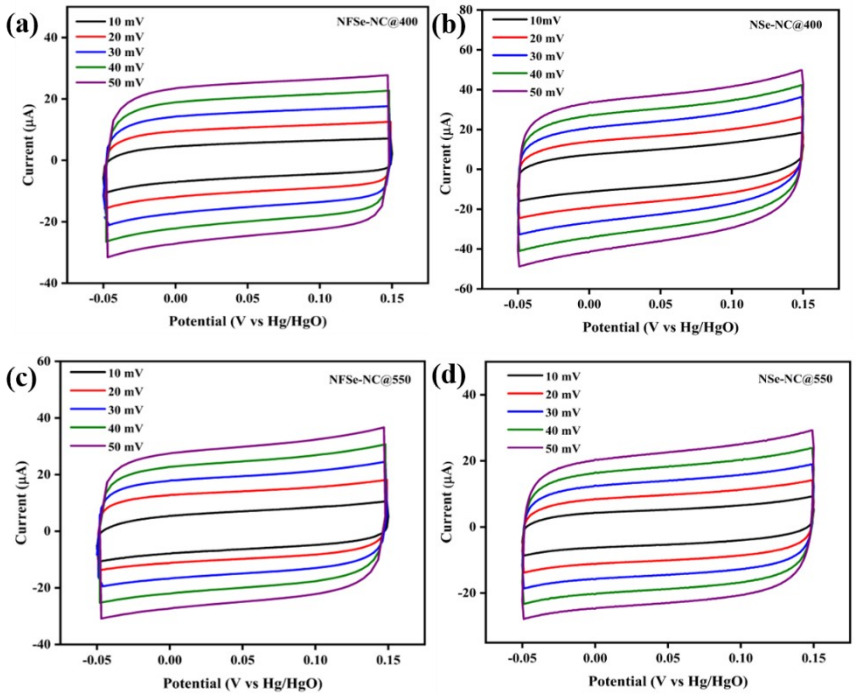

Figure S10. CV curves at various scan rates (a) NFSe-NC@400, (b) NSe-NC@400, (c) NFSe-NC@550, and (d) NSe-NC@550.

ECSA calculation:

Double layer capacitance is calculated by,

C_{dl}= ½ (j_a-j_c), j_a and j_c is anodic and cathodic current density

Slope obtained from capacitive current against scan rates (Fig. 6d) is used to calculate C_{dl}

For, NFSe-NC@400, Slope = j_a-j_c = 971 μF; C_{dl} = ½ (971) = 485.5 μF cm^{-2}

NSe-NC@400, Slope = j_a-j_c = 1370 μF; C_{dl} = ½ (1370) = 685 μF cm^{-2}

NFSe-NC@550, Slope = j_a-j_c = 1028 μF; C_{dl} = ½ (1028) = 514 μF cm^{-2}

NSe-NC@550, Slope = j_a-j_c = 870 μF; C_{dl} = ½ (870) = 435 μF cm^{-2}

Electrochemical Surface Area (ECSA) can be calculated by following the formula

$$ECSA = C_{dl}/C_{sp},$$

C_{sp} represents average specific capacitance, and C_{sp} is of about 40 μF cm^{-2}. [4]

For, NFSe-NC@400, ECSA= 12.13

NSe-NC@400, ECSA= 17.12

NFSe-NC@550, ECSA= 12.85

NSe-NC@550, ECSA= 10.87

Turn Over Frequency (TOF) calculation:

$$TOF = \frac{\frac{J \; x \; SurfaceArea}{4 \; x \; F \; x \; n}}{Mass\ loading}$$

$$n = \frac{}{molecular\ weight}$$

TOF of each active site (s^{-1}) can be calculated by the following equation:

Where J represents current density at 1.49 V, F is the Faraday constant (96485 C mol^{-1}), and n is the number of active sites.

Exchange current density:

Exchange current density is the important parameter for the intrinsic activity of the catalyst and can be calculated by the intersection of the Tafel zone tangent and line of $E = E_0$ (For OER E_0=1.23 V vs RHE).

$$I = I_0\left[\exp\left(\alpha A\frac{nF}{RT}\times\eta\right) - \exp\left(-\alpha C\frac{nF}{RT}\times\eta\right)\right]$$

$$\left|\ln I = \ln I_0 + \left(\frac{\alpha AnF}{RT}\right)\eta\right|$$

Here, I stands for the current density, I_0 is the exchange current density, *i.e.* the current at equilibrium potential, n is the number of electrons involved in the reaction (n=4), F is the Faraday constant (96 485 C mol^{-1}), T is the absolute temperature in Kelvin, η is the overpotential, a_A and a_C are the charge transfer coefficients for anodic reaction (OER), and cathodic reaction (HER) and R is the gas constant.

A higher exchange current density signifies a superior electrocatalyst. This value is determined by extrapolating the linear fit in the Tafel slope, where the equilibrium potential of the OER process intersects the logarithmic current density scale. A higher exchange current density reveals the intrinsic rate of reaction transfer between the electrode and electrolyte under equilibrium conditions. It is influenced by the electrocatalyst material, the analyte in the solution, and the temperature.[5]

Calculation of Faradaic efficiency:

Selectivity is one of the important qualities in electrocatalysis, and it can be screened by faradaic efficiency. A reliable electrochemical technique to determine faradaic efficiency is Rotating Ring Disk Electrode (RRDE). The oxygen molecule evolving from the glassy carbon disk electrode will be reduced to a water molecule by the Platinum ring electrode by applying a constant potential. It is calculated by following the equation,

$$\text{Faradaic efficiency} = I_r \times n_d / I_d \times n_r \times N_{CL}$$

I_r is the ring current, I_d is the disk current, n_d is the number of electrons transferred in disk electrode (n_d=4 electron transferred during OER), n_r is the number of electrons transferred in ring electrode (n_r=4 electron transferred during ORR by Pt electrode) and N_{CL} is collection efficiency.

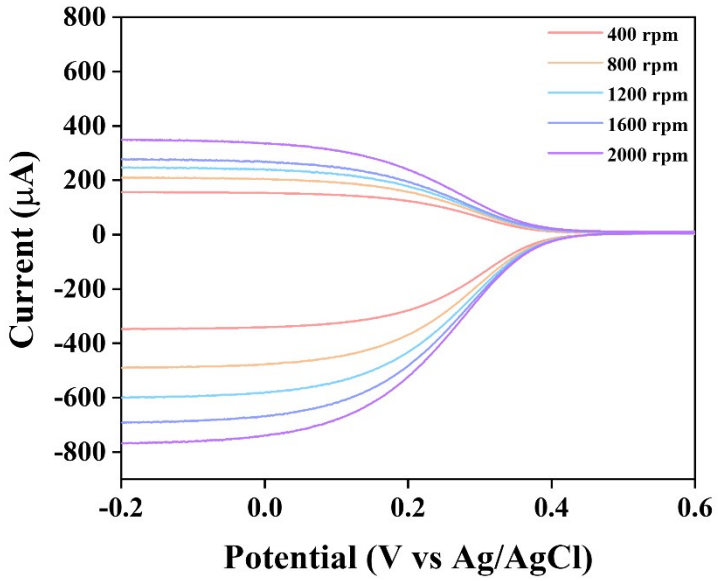

Collection Efficiency determination:

Figure S11. LSV curves for the redox reaction of 10 mM Ferro-ferricyanide in 1M NaOH at various rpm in RRDE

The collection efficiency (N_{CL}) is determined by the redox reaction of 10 mM ferro-ferricyanide using RRDE in 1M NaOH at 5 mV s^{-1} under different rotation rates in an N_2 atmosphere. The N_{CL} is the ratio of ring current to disk current.

$N_{CL} = I_r/I_d$, I_r is the ring current, and I_d is the disk current.

It is determined by taking the I_d and I_r at -0.1V vs Ag/AgCl from the above LSV curves and calculated as $N_{CL} = 0.42$.

NFSe-NC@400:

Faradaic efficiency of NFSe-NC@400 (Fig. 7d) is calculated by applying disk potential (E_d= 1.59V vs RHE) and ring potential (E_r= 0.4V vs RHE) at 1600 rpm and at 150s it is calculated as,

Faradaic efficiency of NFSe-NC@400 = $2.74 \times 10^{-4} / (6.79 \times 10^{-4} \times 0.42)$

Faradaic efficiency of NFSe-NC@400 = 96 %

k-L plot for ORR:

The kinetic parameters of the catalyst during the ORR process were evaluated using a k-L plot, where the inverse of the current density (J^{-1}) is plotted against the inverse of the square root of the rotation speed ($\omega^{-1/2}$) at different potentials. The conversion from rpm to rad/s is provided in Equation S1. The slope of the best linear fit was used to calculate the number of electrons (n) involved in the oxygen reduction process based on the k-L equation.

$$\omega_{(rad\ s^{-1})} = 2\pi/60\ N_{rpm} \quad \textbf{(S1)}$$

$$\frac{1}{J} = \frac{1}{J_L} + \frac{1}{J_k} = \frac{1}{\sqrt{B_\omega}} + \frac{1}{J_k} \quad \textbf{(S2)}$$

$$B = 0.62nFC_0(D_0)^{2/3}v^{-1/6} \quad \textbf{(S3)}$$

Where J is the limiting current density in $A \cdot cm^{-2}$, J_k and J_L are the kinetic and diffusion current density, F is the Faraday constant (96485 $C \cdot mol^{-1}$), C_0 is the saturation concentration of O_2 in 0.1 M KOH (1.2×10^{-6} mol cm^{-3}) at room temperature, D_0 is the diffusion coefficient(1.93×10^{-5} cm^2 s^{-1}) of O_2 and ν is the kinematic viscosity of the electrolyte (0.01 $cm^2 s^{-1}$), ω is the rotation rate, $rad \cdot s^{-1}$. The number of electrons is determined from the slope and J_k using intercept at the y-axis of the k-L plot.[6]

RRDE measurement for calculating n and % of H_2O_2 produced:

Rotating Ring Disk Electrode (RRDE) is also used to determine the number of electrons and % of H_2O_2 yield. It can be calculated by following the equation,

$$n = 4\frac{I_D}{I_D + I_R/N} \quad \textbf{(S4)}$$

$$\%H_2O_2 = 200\frac{I_R/N}{I_D + I_R/N} \quad \textbf{(S5)}$$

I_D is the disk current, I_R is the ring current, and N is the collection efficiency.

In the RRDE experiment, the Pt ring was held at a potential of 1.26 V vs. RHE, covering a wide range of ORR disk potentials.

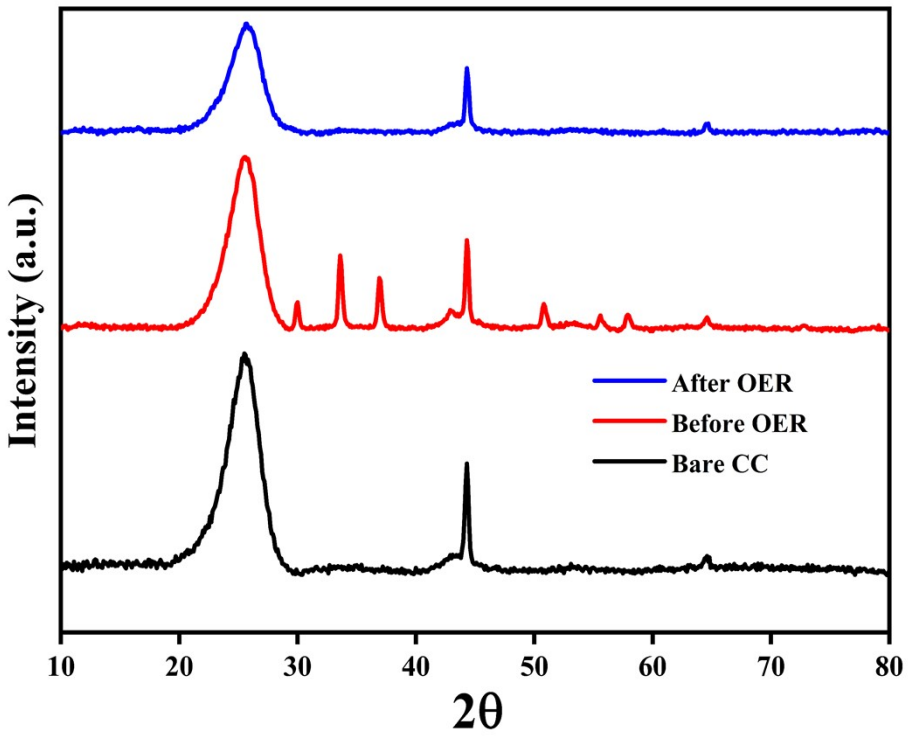

Figure S12. XRD patterns of NFSe-NC@400 before and after the stability test

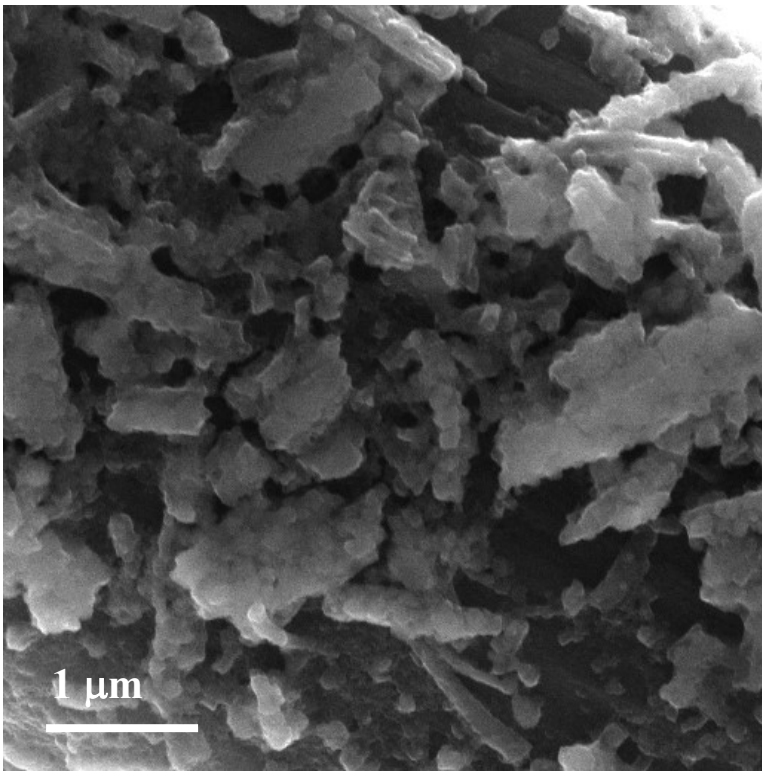

Figure S13. FESEM images of NFSe-NC@400 after the stability test

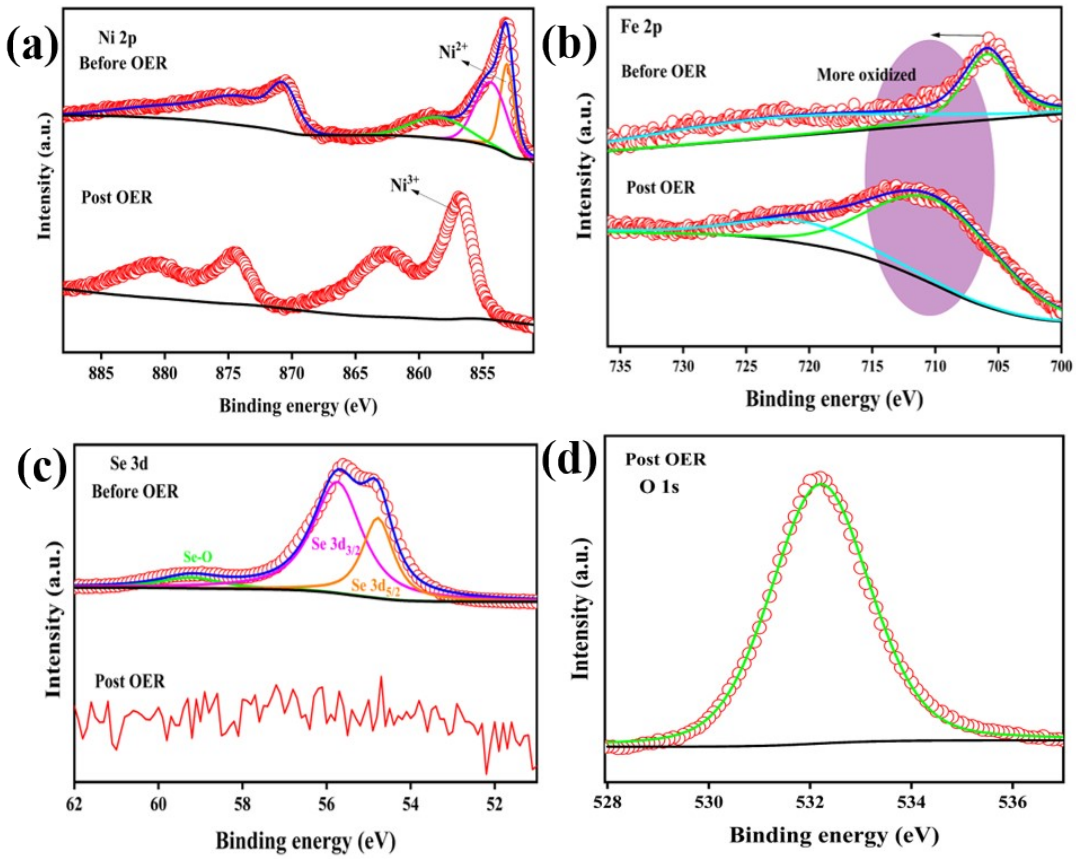

Figure S14. XPS spectrum of (a) Ni 2p, (b) Fe 2p, (c) Se 3d, and (d) O 1s of NFSe-NC@400 before and after the stability test

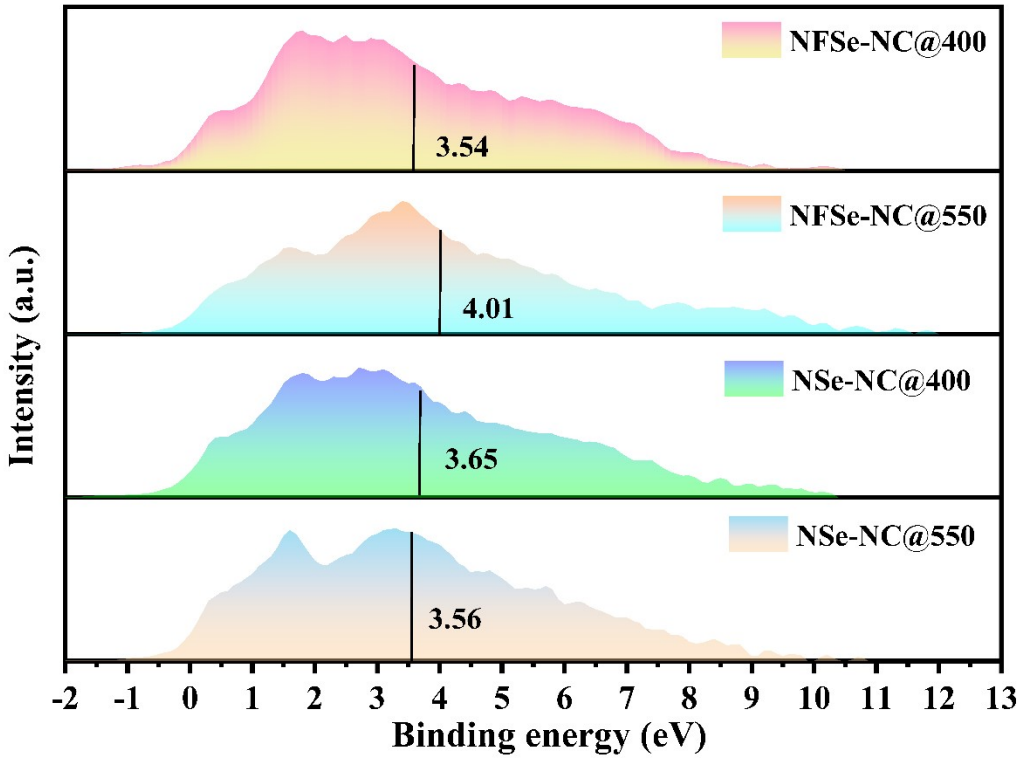

Figure S15. Valence band spectra of NFSe-NC@400, NFSe-NC@550, NSe-NC@400, and NSe-NC@400 measured by XPS.

The d-band center position is marked by the horizontal bar in plots.

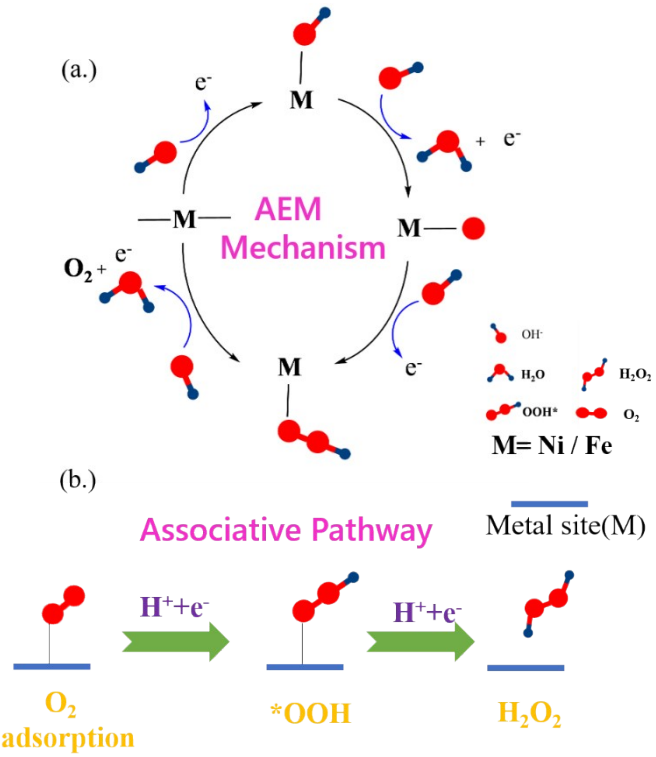

Fig. S16. Proposed Mechanism for (a.) OER (b.) ORR

The probable mechanism and pathway of OER are illustrated in Fig. S16a. The active metal site (Ni/Fe) initially adsorbs OH^- ions, followed by the deprotonation of the hydroxyl ligand coordinated to the catalytic site. This is succeeded by a catalytic oxidation step, leading to the formation of a hydroperoxide intermediate (*OOH). The process ultimately leads to the evolution of O_2 from *OOH through a four-electron transfer mechanism.[7] The expected mechanism and pathway of ORR are illustrated in Fig. S16b. The Oxygen Reduction Reaction (ORR) typically proceeds through either an associative or dissociative pathway, depending on the mode of oxygen adsorption. In the associative pathway, peroxide formation is favored, beginning with the adsorption of the O_2 molecule onto the catalyst surface via the Pauling mode. This is followed by O_2 adsorption facilitating the generation of *OOH. Moderate *OOH adsorption promotes the reaction, whereas stronger *OOH adsorption leads to unfavorable peroxide formation. The process concludes with the reduction of *OOH to H_2O_2.[8]

Table S1. Comparison of electrochemical OER performances of various electrocatalysts in 1 M KOH solution.

S.No.	Electrocatalysts	Overpotential (mV) at 10 mA cm^{-2}	Tafel Slope mV/dec	References
1.	$Fe_{0.25}Ni_{0.75}Se_2$	275	74.8	[9]
2.	$NiSe_2$/CFP	280	81	[10]
3.	MOF derived Fe doped $Ni_3Se_4/NiSe_2$	294	49.02	[11]
4.	$NiSe_2$-FeSe-DHPs	280	58	[12]
5.	Fe-NiS_2@NC	255	65	[13]
6.	MOF derived Ni-Fe-Se/CFP	281	40.93	[14]
7.	$Ni_{0.75}Fe_{0.25}$ Se_2 nanosheets/CFC	255	47.2	[15]
8.	$Ni_xFe_{1-x}Se_2$ porous-nano-microspheres	285	90	[16]
9.	$Ni_xCo_{1-x}Se_2$ hollow micro-particles	320	78	[17]
10.	Ni_x Fe_{1-x} Se_2 -NC@400	253	57.1	This work

Table S2. Comparison of electrochemical ORR performances of various electrocatalysts in 0.1 M KOH solution.

S.No.	Electrocatalysts	Tafel slope mV/dec	References
1.	$Ni_{1-x}Se$	55	[18]
2.	$Ni_{0.85}Se/Co_{0.85}Se$-NHCS	58.2	[19]
3.	$NiCo_2S_4$@NiFe LDH	46.5	[20]
4.	NC@Co-NGC DSNCs	51	[21]
5.	Fe_2NiSe_4@Fe-NC	107.6	[22]
6.	NiFe/N-doped 3D porous carbon nanosheet	84	[23]
7.	NiFe-NC	63	[24]
8.	$Ni_x\ Fe_{1-x}\ Se_2$ -NC@400	34.8	This work

References:

1 L. Yu, S. Sun, H. Li and Z. J. Xu, *Fundamental Research*, 2021, **1**, 448–452.

2 W. Xie, Z. Li, S. Jiang, J. Li, M. Shao and M. Wei, *Chemical Engineering Journal*, 2019, **373**, 734–743.

3 S. Anantharaj and S. Noda, *Mater Today Energy*, 2022, **29**, 101123.

4 C. C. L. McCrory, S. Jung, J. C. Peters and T. F. Jaramillo, *J Am Chem Soc*, 2013, **135**, 16977–16987.

5 A. Raveendran, M. Chandran and R. Dhanusuraman, *RSC Adv*, 2023, **13**, 3843–3876.

6 T. Radhakrishnan, M. P. Aparna, R. Chatanathodi and N. Sandhyarani, *ACS Appl Nano Mater*, 2019, **2**, 4480–4488.

7 A. Raveendran, M. Chandran and R. Dhanusuraman, *RSC Adv*, 2023, **13**, 3843–3876.

8 M. Song, W. Liu, J. Zhang, C. Zhang, X. Huang and D. Wang, *Adv Funct Mater*, 2023, **33**, 2212087.

9 A. Kareem and S. Senthilkumar, *Int J Hydrogen Energy*, 2023, **48**, 7374–7384.

10 L. Zhai, C. H. Mak, J. Qian, S. Lin and S. P. Lau, *Electrochim Acta*, 2019, **305**, 37–46.

11 K. Srinivas, F. Ma, Y. Liu, Z. Zhang, Y. Wu and Y. Chen, *ACS Appl Mater Interfaces*, 2022, **14**, 52927–52939.

12 S. K. Ramesh, V. Ganesan and J. Kim, *ACS Appl Energy Mater*, 2021, **4**, 12998–13005.

13 F. Wen, L. Pang, T. Zhang, X. Huang, C. Li and H. Liu, *Int J Hydrogen Energy*, 2024, **57**, 263–272.

14 Y. Guo, C. Zhang, J. Zhang, K. Dastafkan, K. Wang, C. Zhao and Z. Shi, *ACS Sustain Chem Eng*, 2021, **9**, 2047–2056.

15 Z. Wang, J. Li, X. Tian, X. Wang, Y. Yu, K. A. Owusu, L. He and L. Mai, *ACS Appl Mater Interfaces*, 2016, **8**, 19386–19392.

16 Y. Li, R. Chen, D. Yan and S. Wang, *Chem Asian J*, 2020, **15**, 3845–3852.

17 D. V. Shinde, L. De Trizio, Z. Dang, M. Prato, R. Gaspari and L. Manna, *Chemistry of Materials*, 2017, **29**, 7032–7041.

18 H. Zhang, S. Zheng, J. Tang, R. Chen, J. Yang, W. Tong and J. Guo, *New Journal of Chemistry*, 2023, **47**, 11675–11684.

19 L. J. Peng, J. P. Huang, Q. R. Pan, Y. Liang, N. Yin, H. C. Xu and N. Li, *RSC Adv*, 2021, **11**, 19406–19416.

20 X. Feng, Q. Jiao, W. Chen, Y. Dang, Z. Dai, S. L. Suib, J. Zhang, Y. Zhao, H. Li and C. Feng, *Appl Catal B*, 2021, **286**, 119869.

21 S. Liu, Z. Wang, S. Zhou, F. Yu, M. Yu, C.-Y. Chiang, W. Zhou, J. Zhao, J. Qiu, S. H. Liu, Z. Y. Wang, M. Z. Yu, J. S. Qiu, S. Zhou, J. J. Zhao, F. J. Yu, C. Chiang and W. Z. Zhou, *Advanced Materials*, 2017, **29**, 1700874.

22 S. Ibraheem, S. Chen, L. Peng, J. Li, L. Li, Q. Liao, M. Shao and Z. Wei, *Appl Catal B*, 2020, **265**, 118569.

23 X. Lu, M. Wu, Z. Lu, J. Hu, J. Xie, A. Hao and Y. Cao, *J Alloys Compd*, 2023, **942**, 169095.

24 B. Ricciardi, W. da Silva Freitas, B. Mecheri, K. U. Nisa, J. Montero, V. C. A. Ficca, E. Placidi, C. Alegre and A. D'Epifanio, *Carbon N Y*, 2024, **219**, 118781.